J. Fluid Mech. (2006), *vol.* 565, *pp.* 171–195.
doi:10.1017/S0022112006001558 Printed in the United Kingdom

The effect of confinement on the stability of two-dimensional shear flows

By MATTHEW P. JUNIPER

Department of Engineering, University of Cambridge,
Trumpington Street, Cambridge, CB2 1PZ, UK

(Received 9 September 2005 and in revised form 17 March 2006)

It has been shown recently that the instability of a two-dimensional wake increases when it is confined in the transverse direction by two flat plates. Confinement causes the transition from convective to absolute instability to occur at lower values of shear. This paper examines this effect comprehensively and concludes that it is due to the constructive interaction of modes with zero group velocity in the wake (or jet) and in the surrounding flow. Maximum instability occurs when the wavenumber of the fundamental mode in the wake (or jet) matches that of the fundamental mode in the surrounding flow. Other regions of high instability occur when the harmonics of one mode interact with the fundamental of the other. This effect is examined at density ratios from 0.001 to 1000. At each density ratio, the confinement which causes maximum absolute instability can be predicted. This study also shows that it is vital to examine the wavenumber of absolutely unstable modes in order to avoid over-predicting the absolute instability. In some situations this wavenumber is vanishingly small and the mode must be discounted on physical grounds.

1. Introduction

This paper describes the effect of confinement on the stability of two-dimensional jets and wakes. These flows consist of a central sheet of one fluid sandwiched between two identical sheets of another fluid. All sheets have infinite extent in the flow direction, but the outer sheets are confined in the transverse direction by two plates, as shown in figure 1. If the inner fluid moves faster than the outer fluid, it is a jet flow. If the outer fluid moves faster than the inner fluid, it is a wake flow.

Unconfined shear flows have already been extensively studied. Two common examples are the two-dimensional bluff-body wake and the axisymmetric low-density jet. Previous theoretical and experimental work on these configurations is reviewed by Huerre & Monkewitz (1990, § 6). A region of local absolute instability exists in the immediate wake of a two-dimensional bluff body. This can lead to an unstable global shear mode that is the cause of vortex shedding. The same process occurs in hot jets. The key point is that a local region of absolute instability causes the flow to act as a self-excited oscillator, rather than as an amplifier of extrinsic perturbations, the latter being characteristic of a convectively unstable flow.

The effect of viscosity, velocity profile and density ratio on the stability of unconfined two-dimensional jets and wakes was studied by Yu & Monkewitz (1990). They concluded that the transition to absolute instability is caused by an interaction between the two shear layers and is not a viscous effect. They also found that

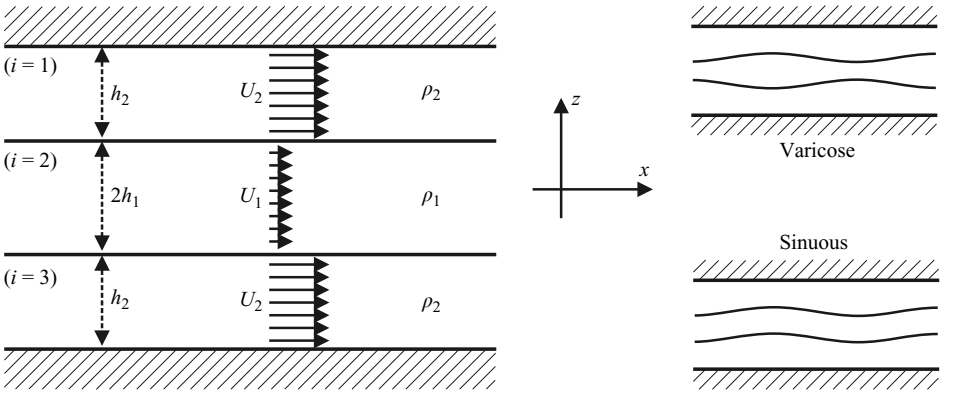

FIGURE 1. The model consists of three flows sandwiched between two flat plates. The outer flows are identical. Each fluid has a constant density and a uniform velocity.

low-density jets and high-density wakes become absolutely unstable at lower values of shear than the same flows at uniform density. The present paper starts by extending figure 2 of Yu & Monkewitz to higher density ratios and then considers the effect of confinement.

Until recently, the effect of confinement seems to have been largely overlooked. An early experiment by Shair *et al.* (1963) on the onset of self-excited fluctuations behind a cylinder in a duct found that confinement stabilizes the flow. This experiment was at Reynolds numbers between 40 and 140. However, an experiment at $Re = 45\,000$ by Bearman & Zdravkovich (1978) on the flow around a cylinder placed next to a wall found that the vortex-shedding frequency becomes better defined as the cylinder approaches the wall. This indicates that the global shear mode is less sensitive to external noise, which suggests that this semi-confined configuration exhibits a stronger absolute instability. A numerical study at two values of confinement by Delbende & Chomaz (1998) found that the sinuous motion of a confined two-dimensional wake is more unstable than that of a weakly confined wake. Juniper & Candel (2003) then showed in a theoretical study that inviscid jets and wakes become absolutely unstable over a wider range of shear when they are confined. The latter study was motivated by the observation that confined fuel injectors produce good mixing with a low pressure drop (Barrère *et al.* 1960). Juniper & Candel proposed that this is because the flow is absolutely unstable in the confined region and stimulates a global mode with large-scale sinuous motion that aids mixing. However, neither Delbende & Chomaz nor Juniper & Candel explained the effect in terms of the interaction of the inner and outer streams, which is the subject of this paper.

The present study employs a linear spatio-temporal stability analysis to determine theoretically the convective/absolute instability of confined jets and wakes as a function of shear, density ratio and confinement. Linear analyses of these configurations are surprisingly successful at predicting the onset of global modes (Delbende & Chomaz 1998), so a nonlinear analysis is not attempted here. The fluids are assumed to be inviscid and to have plug velocity profiles because the aim is to isolate the effect of confinement rather than to represent a realistic flow. Nevertheless, Yu & Monkewitz (1990) have shown that this will give a reasonable prediction of the convective/absolute transition because this is relatively unaffected by the viscosity and the exact shear-layer profile above $Re \sim 1000$. The advantage of this approach is that the dispersion relation can be expressed with ω as an analytic function of

k. Contours of ω in the k-plane can therefore be generated easily and the nature of all saddle points determined by inspection of this two-dimensional manifold. The manifold that represents the confined flow can then be compared with the manifolds of the individual flows when unconfined to obtain a physical understanding of the effect of confinement. It is shown that the strong effect of confinement is due to resonance between modes with zero group velocity in the inner and outer flows.

Section 2 describes the model and the derivation of its dispersion relation. Section 3 introduces the local stability analysis and describes the procedure used in this study to identify absolutely unstable flows. Section 4 examines the effect of density ratio and shear in an unconfined situation, extending to density ratios much higher than those currently available in the literature. Sections 5 and 6 explore the effect of confinement on varicose and sinuous perturbations in a uniform fluid, carefully deducing the physical mechanisms behind this effect. Section 7 evaluates the effect of confinement on jets and wakes over a wide range of density ratios and § 8 explores its implications.

2. Dispersion relations of confined shear flows

The model shown in figure 1 is chosen because it exhibits confinement but is simple to analyse. Three flows with infinite extent in the x-direction are sandwiched between two flat plates. The inner flow has thickness $2h_1$ in the z-direction, density ρ_1 and uniform velocity U_1. The outer flows both have thickness h_2 in the z-direction, density ρ_2 and uniform velocity U_2. The surface tension at the interfaces is σ and the fluids are inviscid.

Small perturbations are superimposed onto the uniform flows described above. The linearized equations of motion are then derived via the classic normal mode decomposition summarized in the next paragraph. When combined with the boundary conditions, these equations of motion reduce to a single equation that relates the complex angular frequency, ω, of each normal mode to its complex wavenumber, k. This equation, the dispersion relation, serves two purposes: it must be satisfied for the equations of motion and boundary conditions to be satisfied; and it gives the phase velocity and group velocity of the permitted perturbations. The group velocity is used in the spatio-temporal analysis described in § 3. Thus the analysis of the model reduces entirely to the analysis of its dispersion relation.

The three flows are irrotational with velocity potentials $\Phi_i(x, z, t) = U_i x + \varphi_i(z)\mathrm{e}^{\mathrm{i}(kx-\omega t)}$, $i = 1, 2, 3$. The three equations of motion, $\nabla^2\Phi_i = 0$, constrain the three functions, $\varphi_i(z)$, to be of the form $\varphi_i(z) = A_i\mathrm{e}^{kz} + B_i\mathrm{e}^{-kz}$. This creates six unknowns, (A_i, B_i), that reduce to three when we consider either varicose perturbations, where the shear layers move as mirror images of each other, or sinuous perturbations, where the shear layers move parallel to each other. Any perturbation can be formed from a linear combination of a varicose and a sinuous perturbation. Having taken advantage of this symmetry we may now consider just one half of the model, where there are three further constraints: (*a*) imposition of zero z-velocity at the confining wall, (*b*) continuity of particle displacement at the interface and (*c*) equating the pressure difference across the interface with the product of curvature and surface tension. These three constraints eliminate the three unknowns, so the equations of motion and boundary conditions reduce to a single relationship between ω, k and the flow parameters (U_i, ρ_i, h_i). As already explained, this dispersion relation can only be satisfied for certain eigenvalues, (ω, k), from which the corresponding eigenfunctions, $\varphi_i(z)$, can be calculated. Further details can be found in Drazin & Reid (1981, § 4).

In dimensional terms, the varicose and sinuous dispersion relations for the model in figure 1 are, respectively:

$$D \equiv \rho_1(U_1 - \omega/k)^2 \coth(kh_1) + \rho_2(U_2 - \omega/k)^2 \coth(kh_2) - k\sigma = 0,$$
$$D \equiv \rho_1(U_1 - \omega/k)^2 \tanh(kh_1) + \rho_2(U_2 - \omega/k)^2 \coth(kh_2) - k\sigma = 0.$$

The following reference scales are now defined: velocity, $U_{ref} \equiv (U_1 + U_2)/2$; length, h_1; density, ρ_2. The dimensionless variables are $k^* \equiv kh_1$ and $\omega^* \equiv \omega h_1/U_{ref}$. The dimensionless parameters are $\Lambda \equiv (U_1 - U_2)/(U_1 + U_2)$, $S \equiv \rho_1/\rho_2$, $h \equiv h_2/h_1$ and $\Sigma \equiv \sigma/(h_1\rho_2 U_{ref}^2)$. The varicose and sinuous dispersion relations become:

$$D^* \equiv S(1 + \Lambda - \omega^*/k^*)^2 \coth(k^*) + (1 - \Lambda - \omega^*/k^*)^2 \coth(k^*h) - k^*\Sigma = 0,$$
$$D^* \equiv S(1 + \Lambda - \omega^*/k^*)^2 \tanh(k^*) + (1 - \Lambda - \omega^*/k^*)^2 \coth(k^*h) - k^*\Sigma = 0.$$

The dispersion relations for the unconfined case are found by letting h tend to infinity so that $\coth(k^*h)$ tends to unity for $k_r^* \neq 0$. In the unconfined case k_r^* must be positive in order to avoid the eigenfunctions tending to infinity as z tends to infinity. This can be achieved by defining $s \equiv \mathrm{sign}(k_r^*)$ and writing the relation as:

$$D^* \equiv S(1 + \Lambda - \omega^*/k^*)^2 \coth(sk^*) + (1 - \Lambda - \omega^*/k^*)^2 - sk^*\Sigma = 0,$$
$$D^* \equiv S(1 + \Lambda - \omega^*/k^*)^2 \tanh(sk^*) + (1 - \Lambda - \omega^*/k^*)^2 - sk^*\Sigma = 0.$$

The only characteristic length scale for a single shear layer is that determined by the surface tension: $\sigma/(\rho_2 U_{ref}^2)$. Therefore $k^* \equiv k\sigma/(\rho_2 U_{ref}^2)$, $\omega^* \equiv \omega\sigma/(\rho_2 U_{ref}^3)$ and the dispersion relation is simply:

$$D \equiv S(1 + \Lambda - \omega^*/k^*)^2 + (1 - \Lambda - \omega^*/k^*)^2 - sk^* = 0.$$

Both dimensional and non-dimensional frameworks are used in this article because physical phenomena are best explained dimensionally and mathematical features are best explained non-dimensionally. All of the figures and most of the text is in the non-dimensional framework. Non-dimensional variables are denoted by an asterisk where the framework could be ambiguous.

3. Spatio-temporal instability analysis

3.1. *Definition of locally convective and locally absolute instability*

The local instability characteristics of a flow are determined by considering its response to a point-source impulse. If the resulting perturbation dies away everywhere, the flow is stable. If it is amplified, a further distinction is necessary between convectively unstable flows and absolutely unstable flows. The former produce wave packets that convect away from the source. The latter produce wave packets that expand around the source and that eventually contaminate the entire flow.

Convective instability and absolute instability are distinguished by examining the dispersion relation's solutions that have zero group velocity and that satisfy the pinch criterion. A definition of the pinch criterion and a convenient geometric method of finding the solutions with zero group velocity are described in § 3.2. If the flow is unstable but none of the solutions with zero group velocity has positive growth rate, then the flow is convectively unstable. However, if a solution with zero group velocity has positive growth rate, then it will dominate the impulse response and the flow will be absolutely unstable. These concepts have been reviewed comprehensively by Huerre & Monkewitz (1990), Huerre (2000) and Chomaz (2005).

3.2. *Geometric approach to the identification of local absolute instability*

This section describes a geometric approach to identifying values of ω and k that (a) satisfy the dispersion relation, (b) have zero group velocity (i.e. for which $\partial\omega/\partial k = 0$) and ($c$) satisfy the pinch criterion. The example used here is a confined varicose perturbation of a two-dimensional double shear layer, but the same approach is used for the other flows.

The general form of the dispersion relation is $D(\omega, k; P) = 0$, where P is a set of parameters. For a given P there are four unknowns because ω and k are complex. There are two constraints: $\mathrm{Re}(D) = 0$ and $\mathrm{Im}(D) = 0$. Hence the solution $D = 0$ is a two-dimensional manifold in four-dimensional $(\omega_r, \omega_i, k_r, k_i)$ space. Sections 4 to 7 of this paper examine how the shape of this manifold changes as the parameters change and from this the behaviour of the flow is determined.

The general characteristics of the manifolds can be determined by inspection. In all of the dispersion relations, ω can be expressed as an explicit function $\omega(k) = f(k) \pm \sqrt{g(k)}$, where $f(k)$ and $g(k)$ are both singly valued. The function $\omega(k)$ is analytic and, owing to the square root, it has two values of ω for each value of k except at certain well-defined points. Consequently, ω-space is mapped conformally to two Riemann surfaces in k-space. These Riemann surfaces meet where $g(k)$ is zero, at branch points of order 1. Branch cuts can be defined between arbitrary pairs of branch points because there are only two Riemann sheets.

For example, figure 2 shows ω_i-contours of one of these Riemann surfaces in k-space for a confined varicose jet between two fluids with equal density and non-zero surface tension: $P \equiv (S, \Lambda, h, \Sigma) = (1, 1, 1.3, 1)$. The other Riemann surface is a mirror image in the k_i-axis and is not shown here. The manifold is hyperbolic and consequently there are no analytic maxima or minima. It follows that $\partial\omega/\partial k$ can only be zero at a saddle point. Since it is a conformal mapping, contours of ω_r and ω_i remain orthogonal except at branch points and poles of the manifold. Put together this means that if $\partial\omega_i/\partial k$ is zero at any analytic point on the manifold then this point must be a saddle point and $\partial\omega_r/\partial k$ must also be zero. We can therefore plot contours of ω_i in k-space and deduce that all observed saddle points correspond to wavenumbers with zero group velocity.

The large-time impulse response is evaluated by integrating along a path that runs from $k_r = -\infty$ to $k_r = +\infty$. This path originally lies along the k_r-axis, but the integral is more easily evaluated by deforming the path into the $k_i < 0$ half-plane (or the $k_i > 0$ half-plane for flows with negative net mass flux). The path must pass over the steepest descent line of saddle points without being deformed through branch points or through poles of ω_i. Strictly speaking, it should follow lines of constant ω_r in order to avoid oscillating terms, but this condition can be relaxed at large negative ω_i with negligible contribution to the integral. The deformed path is the thick white line in figure 2. It passes over saddles s_1 and s_3, where the dominant contribution comes from s_1 because it has a higher value of ω_i. For these parameter values, the path misses the s_2 family of saddles and they make no contribution to the integral. From a physical point of view, the position of saddle s_1 is controlled by the surface tension, Σ, while the positions of saddles s_2 and s_3 are controlled by the confinement, h. At $\Sigma = 1$, we see that saddle s_1 dominates over s_3 and that the s_2 family of saddles does not contribute to the impulse response. Therefore we can conclude that confinement has little effect on varicose perturbations around $\Sigma = 1$.

An equivalent description of this is the pinch criterion (Briggs 1964), which says that a saddle point contributes to the integral only if the hill on one side consists of upstream-propagating k^+ branches and the hill on the other side consists of

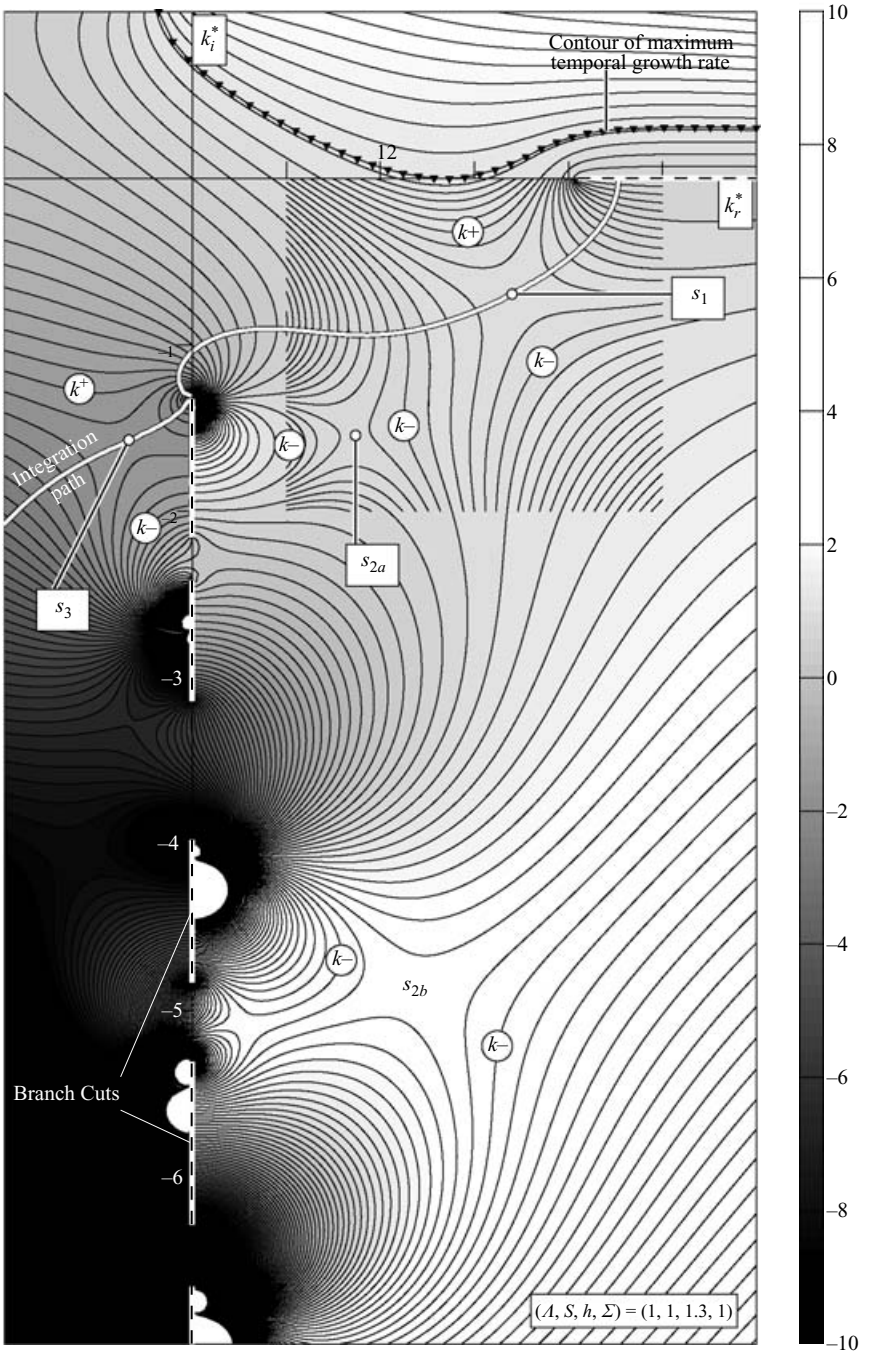

FIGURE 2. Solutions to the dispersion relation $D(\omega, k; \Lambda, S, h, \Sigma) = 0$ for varicose perturbations in a uniform density flow with non-zero surface tension. They are represented as contours of ω_i in the k-plane. Although not shown, contours of ω_r are orthogonal to those of ω_i. The saddle points are solutions with $\partial\omega/\partial k = 0$ and therefore represent modes with zero group velocity. Saddles s_1 and s_3 lie on the integration path and are therefore k^+/k^- pinch points. Saddles s_{2a} and s_{2b} are not on the integration path and are therefore k^-/k^- pinch points. Saddle s_1 is higher than s_3 and if it has positive growth rate, then the flow is locally absolutely unstable. The position of saddle s_1 is controlled by the surface tension, Σ, and the positions of saddles s_2 and s_3 are controlled by the confinement, h.

downstream-propagating k^- branches. It can be seen in figure 2 that the integration path traverses only this type of saddle point. If the saddle point is in the $k_i < 0$ half-plane, then k^+ branches are defined as those that are entirely located in the $k_i > 0$ half-plane for values of ω_i greater than the maximum temporal growth rate, the triangular contour in figure 2. Conversely, the k^- branches must remain in the $k_i < 0$ half-plane as ω_i increases. Hence in figure 2, saddles s_1 and s_3 are k^+/k^- pinch points, but saddles s_{2a} and s_{2b} are k^-/k^- pinch points. Only the k^+/k^- pinch points contribute to the integral.

A comprehensive description of the evaluation of the impulse response has been included because it is important to show why the s_2 family of saddle points become k^+/k^- pinch points and therefore do contribute to the integral when the surface tension tends to zero. As a final point, the s_3 saddles always have lower ω_i than the s_2 saddles and they will not be referred to again in this paper.

The procedure for identifying absolutely unstable regions of parameter space is as follows: (*a*) for a set of parameter values, P, contours of ω_i in k-space are generated for both Riemann surfaces by solving the dispersion relation with Matlab; (*b*) the k^+/k^- saddle points are identified by eye and their exact positions found by solving $D = 0$ and $\partial D/\partial k = 0$ in Matlab; (*c*) if the highest value of ω_i at a saddle point is positive, then the flow is absolutely unstable. In practice, once a saddle point has been identified its position in (ω, k)-space is tracked as the parameter values are changed incrementally. It is necessary to inspect the manifold only when doubt arises over whether a saddle point is still a k^+/k^- pinch point. A further increase in speed is achieved by adding the constraint $\omega_i = 0$ at the saddle point, thus directly identifying the transition line between absolute and convective instability in parameter space.

3.3. *Limit of zero surface tension*

In §§4 to 7, the surface tension is set to zero, which means that there is no stabilizing mechanism and therefore that ω_i tends to infinity as k_r tends to infinity. It then becomes impossible for the impulse response to be zero at times preceding the impulse itself, which obviously violates causality (see Huerre 2000 §3.3 for a detailed explanation of this apparent paradox). This problem is resolved by including surface tension, but letting it tend to zero. The start of this progression is shown in figure 3. The integration path must follow lines of constant ω_r except at very low values of ω_i where it can hop to a different value of ω_r. It must also pass above the top branch point on the k_i-axis which means that it has to traverse saddle s_{2a}. Similarly, it has to traverse saddles s_{2b}, s_{2c} etc. as the surface tension reduces further. Equivalently, we can say that the s_2 family of saddle points become k^+/k^- pinch points as the surface tension tends to zero.

Although saddle s_1 remains the most unstable k^+/k^- pinch point and would dominate the linear impulse response, it moves to very high k_r as the length scale associated with surface tension, $\sigma/(\rho_2 U_{ref}^2)$, tends to zero. In a nonlinear analysis it would saturate at an amplitude as small as its wavelength, which is vanishingly small. With this mode saturated, the dominant contribution to the impulse response in the rest frame comes from the next most unstable k^+/k^- pinch point, namely saddle s_{2a}. Thus it is permissible to set the surface tension to zero and examine the relevant s_2 saddles as long as their wavelength is much greater than $\sigma/(\rho_2 U_{ref}^2)$. This procedure is followed in §§4 to 7.

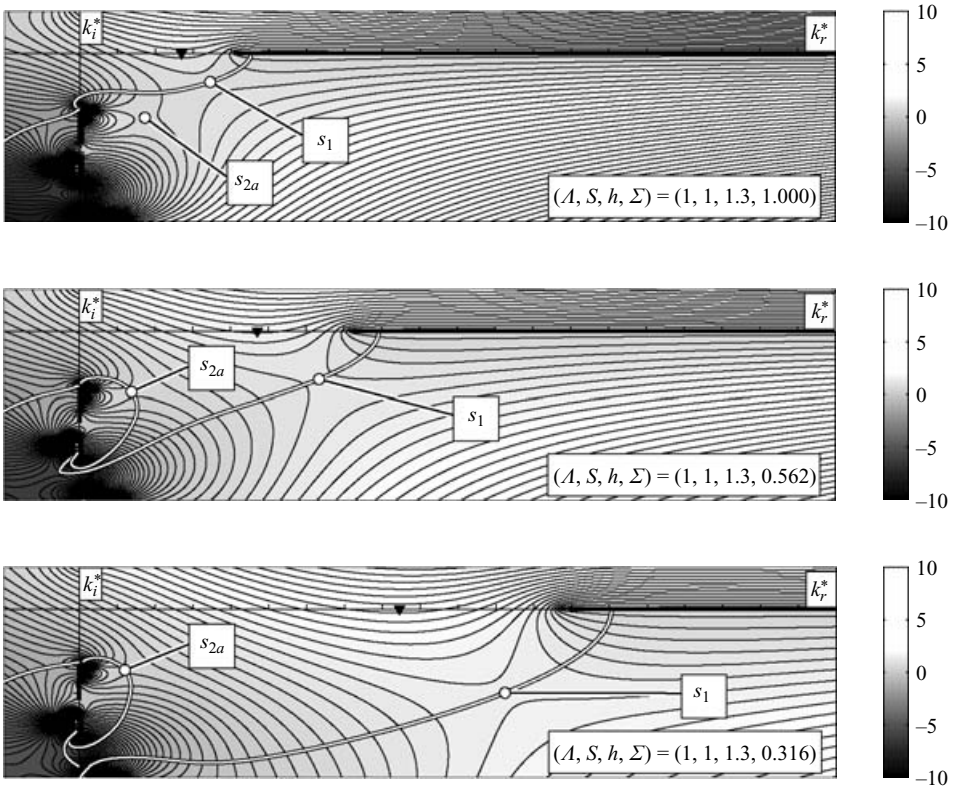

FIGURE 3. Contours of $\omega_i(k)$ for the same flow conditions as figure 2, but with decreasing surface tension. As the surface tension decreases, the integration path (white line) traverses saddle s_{2a} as well as s_1 and therefore they both contribute to the impulse response. Although not shown in this figure, this process continues as the surface tension tends to zero and the integration path traverses all the s_2 saddles shown in figure 4(a). The maximum growth rate predicted via a temporal analysis is shown by a triangle. It remains dominated by surface tension.

3.4. *Relationship with a temporal analysis*

A temporal instability analysis, in which k is real, corresponds to a slice through the k_r axis of the manifold. In figure 2, it predicts that the most unstable wavenumber is $k_r = 1.35$ with growth rate $\omega_i = 0.84$. However, it cannot predict that the mode at saddle s_1 will dominate the large-time impulse response, which is a more relevant result for a physical system. As the surface tension reduces, the most unstable wavenumber in a temporal analysis, shown by a triangle in figure 3, remains dominated by surface tension and is not affected by saddle s_{2a}. Consequently, a temporal analysis does not capture the full effect of confinement, which acts by changing the growth rates of the s_2 saddles that dominate once saddle s_1 has saturated. The s_{2a} saddle does have a very slight effect on the growth rate at small values of k_r which can be seen by careful inspection of the k_r axes of figure 8. However, this is just a shadow of the full effect that is captured by a spatio-temporal analysis, which is why the latter type of analysis is essential here.

4. Effect of density ratio on unconfined shear flows

In many practical situations, the two fluids under consideration have different densities. In this section, the conditions necessary for absolute instability are calculated in terms of the density ratio, S, and shear number, Λ, for unconfined flows. Although this has been reported before by Yu & Monkewitz (1990), their results were only for moderate density ratios ($1/6 < S < 6$). The results presented here extend to density ratios of 1000.

The dispersion relation for unconfined perturbations is:

$$\frac{\rho_1(U_1-\omega/sk)^2}{\rho_2(U_2-\omega/sk)^2}\begin{Bmatrix}\coth(skh_1) & \text{varicose}\\ \tanh(skh_1) & \text{sinuous}\end{Bmatrix} = -1.$$

This equation is symmetric under the transformation (var, ρ_1, U_1) $\leftrightarrow$ (sin, ρ_2, U_2). In this section, the behaviour of the varicose case will be determined using the technique described in § 3.2. Then the behaviour of the sinuous case will be determined by symmetry.

The manifold $D(\omega, k; \Lambda, S) = 0$ has two Riemann surfaces. The surface at higher ω_i for parameter values $(\Lambda, S, \Sigma) = (1, 1, 0)$ is shown in figure 4(a) non-dimensionalized by h_1. The k^- branches repeat along the negative k_i-axis with period $\pi i/h_1$ owing to the periodicity of the $\coth(skh_1)$ term. In the limit of zero surface tension, these all form saddle points with the k^+ branch and all contribute to the impulse response. The saddle point with highest ω_i has an exponentially larger contribution in the long-time limit and the flow is absolutely unstable if this value of ω_i is positive. Whatever the values of ω_i at the saddle points, these modes satisfy $D = 0$ (i.e. they satisfy the equations of motion and the boundary conditions) and $\partial\omega/\partial k = 0$ (i.e. they have zero group velocity). In other words, the flow always supports some modes with zero group velocity, although these modes may be damped. This contrasts with flows that cannot support any modes with zero group velocity, i.e. that have no solutions of $D = 0$ that also satisfy $\partial\omega/\partial k = 0$.

In figure 5, the absolutely unstable region is shown in the (Λ, S)-plane. At density ratios above $S = 0.143$, we discover that saddle s_{2a} is always the most unstable k^+/k^- pinch point, but that its wavenumber, k_r, can be very small. At $(\Lambda, S) = (0.707, 0.143)$, saddle s_{2a} touches the $k_r = 0$ axis and must be discounted for the physical reasons set out in § 5.4. In order to locate the absolutely unstable region in the (Λ, S)-plane, we must impose $k_r = \epsilon$, where $\epsilon \to 0$, which keeps the saddle point in the $k_r > 0$ half-plane. This gives the transition line s'_{2a} in figure 5. At $S = 0.0395$, saddle s_{2b} becomes more unstable and dominates the varicose behaviour. There is no doubt about the validity of s_{2b} because its k_r-value is always of order 1.

For flows with negative net mass flux, $\rho_1 U_1 + \rho_2 U_2$, the integration path lies above the k_r axis and the k^+/k^- pinch points exist in the $k_i > 0$ half-plane. These saddle points are denoted s_{-2a}, s_{-2b} etc. moving up the axis. They are not explicitly plotted in this study because all figures of ω_i contours are plotted at positive net mass flux. For varicose disturbances of flows with negative net mass flux, saddle s_{-2b} is the most unstable saddle point that also has $k_r > 0$. Its convective/absolute transition line is shown in figure 5.

The behaviour of the sinuous mode is deduced by symmetry. The result is the complete map of absolute instability in the $(1/\Lambda, S)$-plane shown in figure 6. Plotting $1/\Lambda$ on the horizontal axis allows the absolutely unstable conditions to be plotted as a single region, which is particularly useful for figures 15 and 16. The results presented

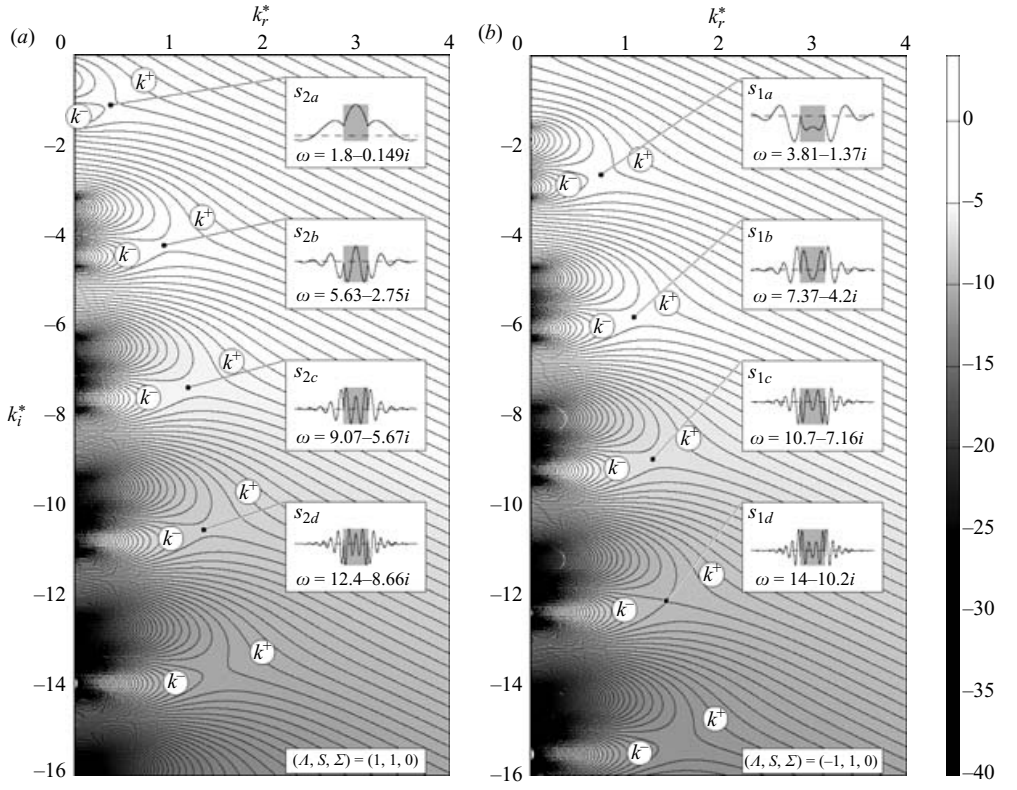

FIGURE 4. Contours of $\omega_i(k)$ for a uniform density unconfined varicose flow without surface tension: (*a*) $\Lambda = 1$, corresponding to a jet in a stationary fluid, and (*b*) $\Lambda = -1$, corresponding to the flow around a stationary wake. The s_1 saddle point in figures 2 and 3 has moved to infinite k_r and therefore does not appear. In (*a*) the s_2 saddles are the same as those in figures 2 and 3, where $\Lambda = 1$. In (*b*) the saddles are equivalent to the s_2 saddles, but correspond to $\Lambda = -1$. In a change of nomenclature these become known as s_1 saddles because this is consistent with § 5, where subscript 1 will refer to the inner flow and subscript 2 will refer to the outer flow. Saddles s_{2a} and s_{1a} are the fundamental modes and the other saddles are harmonics. The pressure eigenfunctions are shown for each mode.

here extend the results of Yu & Monkewitz (1990) and Juniper & Candel (2003) to higher density ratios and recognize the disappearance of the s_{2a} saddle as k_r tends to zero.

5. Effect of confinement on varicose perturbations of a double shear layer in a uniform fluid

This section starts by examining weakly and strongly confined shear flows and demonstrates that they have the same behaviour as unconfined flows. Thus, the inner and outer flows can both support modes with zero group velocity that are stable ($\omega_i < 0$), unstable ($\omega_i > 0$) or marginally stable ($\omega_i = 0$). The behaviour at normal confinement can then be explained in terms of the interaction of the zero group velocity modes in the inner and outer flows.

5.1. *Symmetries of the dispersion relation*

The image system for varicose perturbations of the confined shear flow with $h_1 \sim h_2$ is shown in figure 7(*a*). There is an obvious symmetry under the transformation

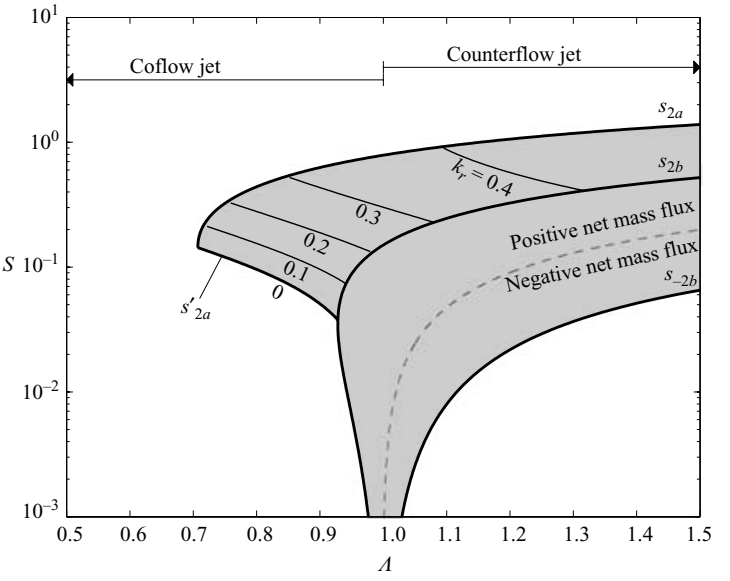

FIGURE 5. Absolutely unstable regions (grey) of an unconfined varicose jet as a function of shear, Λ, and density ratio, S. Each transition line is labelled with the corresponding saddle point. Saddles s_{2a} and s_{2b} are shown in figure 4(a). Saddle s_{-2b} is the second s_2 saddle point above the axis in figure 4(a), but is not shown explicitly. In the region swept out by saddles s_{2b} and s_{-2b}, the wavenumber, k_r, is approximately equal to 1. However, the wavenumber of saddle s_{2a} tends to zero in its absolutely unstable region, as shown by the contours of k_r. When it reaches zero it must be discounted for the reasons given in § 5.4.

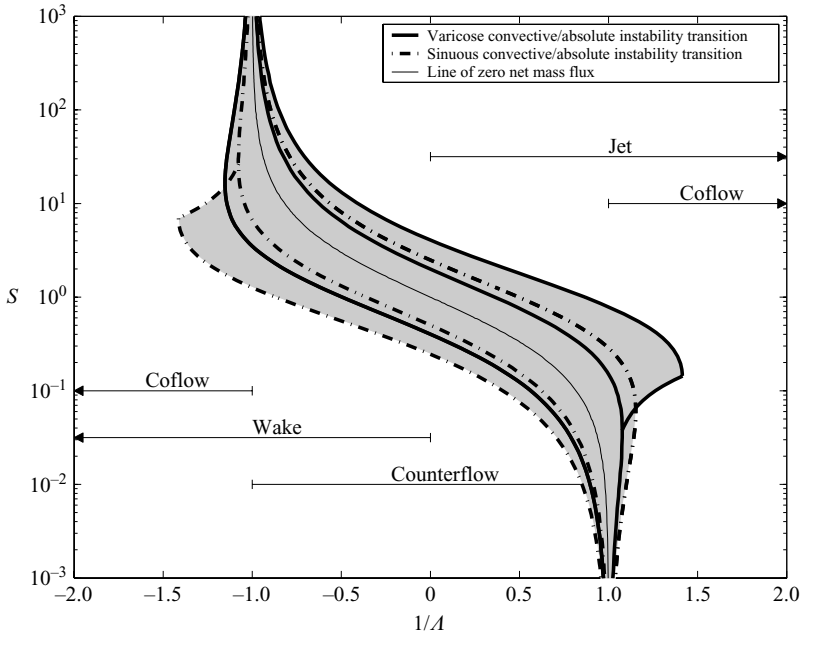

FIGURE 6. Absolutely unstable regions (grey) of varicose and sinuous motions of an unconfined shear flow as a function of shear, Λ, and density ratio, S. Plotting $1/\Lambda$ on the horizontal axis shows the absolutely unstable conditions as a single region and enables better comparison with later figures.

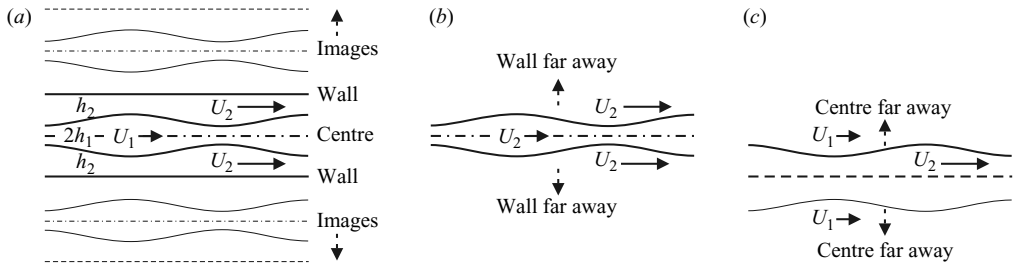

FIGURE 7. Image systems of a confined varicose flow under (*a*) normal confinement, (*b*) weak confinement and (*c*) strong confinement. In flow (*a*) there is an obvious symmetry under the transformation $(U_1, h_1) \leftrightarrow (U_2, h_2)$. Flow (*b*) is similar to an unconfined flow. Flow (*c*) is also similar to an unconfined flow, but with $(U_1, h_1) \leftrightarrow (U_2, h_2)$. Thus for flows (*b*) and (*c*), the zero group velocity modes when $\Lambda = -1$ are given by figures 4(*b*) and 4(*a*), respectively.

$(U_1, h_1) \leftrightarrow (U_2, h_2)$ that can easily be seen in the dispersion relation:

$$D \equiv (U_1 - \omega/k)^2 \coth(kh_1) + (U_2 - \omega/k)^2 \coth(kh_2) = 0.$$

The dispersion relation can be made non-dimensional with either h_1 or h_2 to yield:

$$D^* \equiv (1 + \Lambda - c^*)^2 \coth(k^*) + (1 - \Lambda - c^*)^2 \coth(k^* h) = 0 \quad \text{for } L_{ref} = h_1,$$
$$D^* \equiv (1 - \Lambda - c^*)^2 \coth(k^*) + (1 + \Lambda - c^*)^2 \coth(k^* h) = 0 \quad \text{for } L_{ref} = h_2.$$

Hence, the equivalent symmetry in non-dimensional terms is $(\Lambda, h) \leftrightarrow (-\Lambda, 1/h)$.

5.2. *Implications of behaviour at weak and strong confinement*

When $h_2 \gg h_1$ (weak confinement; $h \gg 1$) the dispersion relation and the image system become like those of the unconfined varicose flow and the effect of the walls is negligible (figure 7*b*). In § 4, it was shown that the unconfined varicose flow can support waves with zero group velocity. For instance, when $\Lambda = +1$, these modes are the saddle points s_{2a} to s_{2d} in figure 4(*a*), which lie at $k_i^* = -(1.113 + n\pi)$, $n = 1, 2, 3$, etc. When $\Lambda = -1$, the zero group velocity modes are the saddle points s_{1a} to s_{1d} in figure 4(*b*), which lie at $k_i^* = -(2.650 + m\pi)$, $m = 1, 2, 3$, etc. The characteristic length is the thickness of the inner flow, h_1, so when $\Lambda = -1$ the zero group velocity modes of the inner flow lie at $k_{i,inner} = -(2.650 + m\pi)/h_1$. The value of k_i is crucial because, from § 2, it is the z-wavenumber of the eigenfunction $\varphi(z) = Ae^{kz} + Be^{-kz}$. In other words, it gives a mode's wavelength in the z-direction. Hence, the z-wavelengths of the zero group velocity modes in the inner flow are proportional to its thickness, h_1 and these modes scale with the inner flow.

On the other hand, when $h_2 \ll h_1$ (strong confinement; $h \ll 1$), the dispersion relation and image system become like those of the unconfined varicose flow with the velocities interchanged, as seen in the transformation $(\Lambda, h) \leftrightarrow (-\Lambda, 1/h)$. The image system is shown in figure 7(*c*). If we were to consider a strongly confined varicose flow with $\Lambda = -1$, the zero group velocity modes in the outer flow would be given by saddle points s_{2a} to s_{2d} in figure 4(*a*). The characteristic length would be h_2 so the zero group velocity modes of the outer flow would be at $k_{i,outer} = -(1.113 + n\pi)/h_2$. Hence, the z-wavelength of the zero group velocity modes in the outer flow would be proportional to its thickness, h_2.

In § 5.3, it will be shown that constructive interference occurs between the zero group velocity modes in each flow when the z-wavelengths of the inner and outer

eigenfunctions match. The values of h for which $k_{i,inner} = k_{i,outer}$ are given by:

$$\Rightarrow h \equiv \frac{h_2}{h_1} = \frac{1.113 + n\pi}{2.65 + m\pi} = 0.092, 0.124, 0.192, 0.420, 1.61, 2.79, 3.98 \ldots \qquad (5.1)$$

For Λ slightly more negative than -1 (i.e. $1/\Lambda$ less negative than -1), it can be seen from figure 11 that less shear is required to generate an absolute instability at precisely these values of h. The most unstable value of h occurs where the fundamental mode in the inner flow, s_{1a}, interacts constructively with the fundamental mode in the outer flow, s_{2a}, at $h = 0.420$.

All the calculations in this section are performed at $\Lambda = -1$ because this facilitates comparison with other sections. Although all the zero group velocity modes of the confined flow are stable when Λ is exactly equal to -1, we can still draw firm conclusions about the unstable flows that occur when Λ is slightly more negative than -1: under these conditions, the ω_i values of the saddle points change in the same way when h varies, but are all higher. Consequently, the saddle points with highest ω_i become unstable, leading to the absolutely unstable regions shown in figure 11.

5.3. *Behaviour at normal confinement*

The manifold of the confined flow for $\Lambda = -1$ is shown in figure 8 at twelve values of confinement, h. It combines features of the weakly confined inner flow (figure 4*b*) and the strongly confined outer flow, (figure 4*a*). As for the unconfined case, the confined manifold $D(\omega, k) = 0$ consists of two Riemann surfaces. Branch points of order 1 occur where $\coth(k)\coth(kh) = 0$ or ∞, which has solutions at $k = n\pi\mathrm{i}/2$ and $k = n\pi\mathrm{i}/2h$. Branch cuts can be taken between arbitrary pairs of branch points because there are only two Riemann surfaces. Again, saddle points are pinched between the k^- branches on the k_i-axis and the k^+ branch coming through the k_r-axis. In the confined case, unlike the unconfined case, the precise location of the k^- peaks on the k_i-axis can be found by setting ω to infinity and solving for k. This is satisfied when $\tanh(k)\coth(kh) = -1$, which has solutions at $k = n\pi\mathrm{i}/(1+h)$. On each Riemann surface, there are two saddle points associated with each peak: one in the $k_r > 0$ half-plane and one in the $k_r < 0$ half-plane. We will study the most unstable of these. For flows with positive net mass flux this lies in the bottom right-hand quadrant of the k-plane. The axes have been multiplied by $(1+h)$ in order to keep approximately the same number of saddle points in each figure and to highlight the nearly symmetric nature of figure 9.

When $h \ll 1$, we can easily identify the saddle points that scale with the inner flow, given by s_{1a} and s_{1b} in figures 4(*b*) and 8(top-left). Similarly, we can identify the saddle point that scales with the outer flow, given by s_{2a} in figures 4(*a*) and 8, under the transformation $h \to 1/h$. When $h \ll 1$, saddle s_{2a} has the highest value of ω_i. The k^- branch corresponding to this saddle has width $k_r \sim 1/h$ and is therefore much wider than the k^- branches associated with the inner flow. The latter branches have $k_r \sim 1$ and can be seen bunched around the $k_r = 0$ axis. Reasoning physically, the wavelength of the dominant eigenfunction, s_{2a}, scales with the width of the thin outer flow and therefore dies down too quickly in the z-direction to be affected by the shear layer on the other side of the inner flow. As h increases, this saddle point and its counterparts s_{2b}, s_{2c} and s_{2d} move along the dotted lines s_{2a}, s_{2b}, s_{2c} and s_{2d} in figure 9, which will be described in more detail later.

Similarly, when $h \gg 1$, we can easily discern the saddle points that scale with the outer flow, given by s_{2a} and s_{2b} in figures 4(*a*) and 8(bottom-right). We can identify the saddle point that scales with the inner flow, given by s_{1a} in figures 4(*b*) and 8.

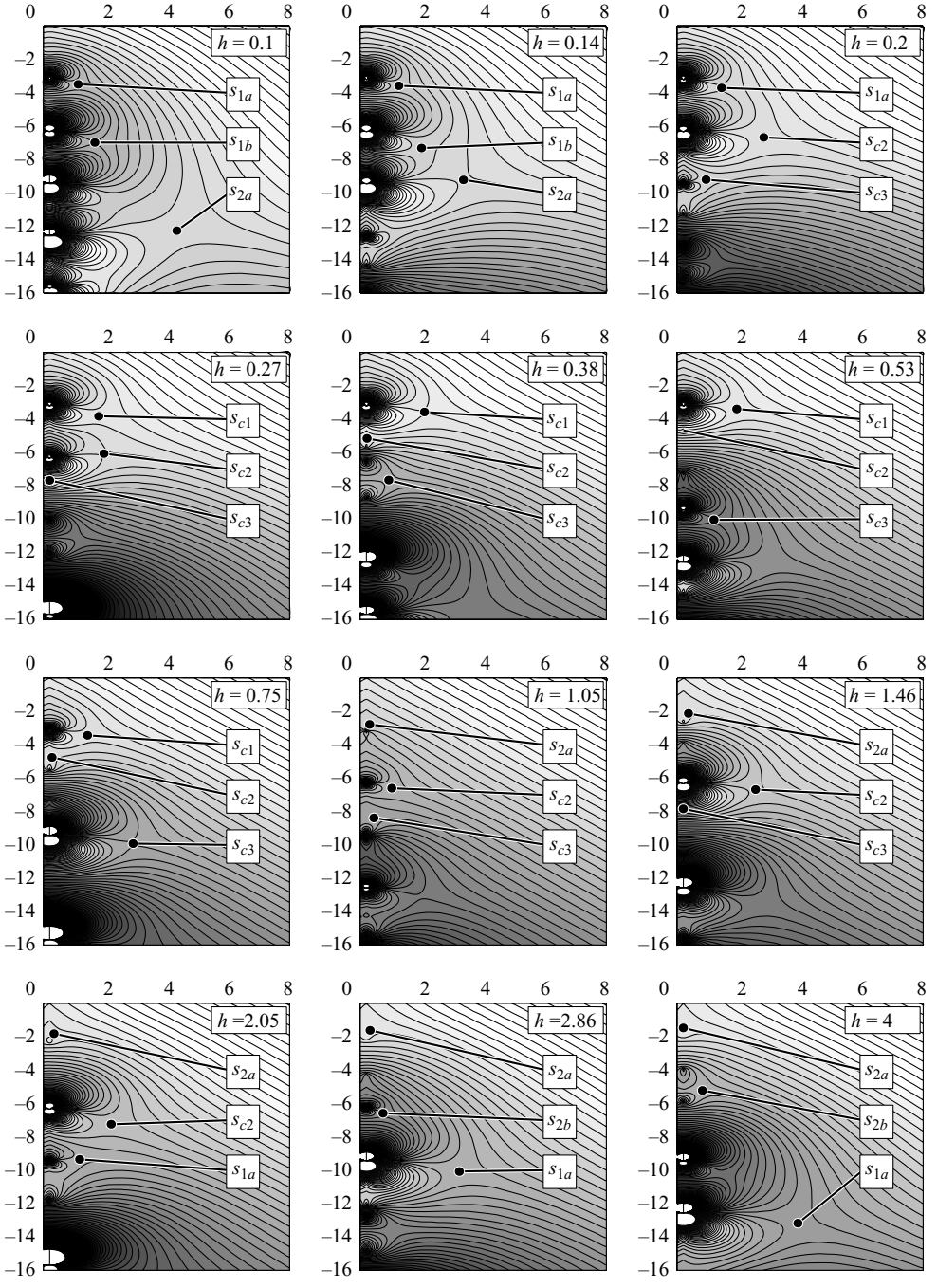

FIGURE 8. Contours of $\omega_i(k)$ for varicose motion of a confined wake flow with $(\Lambda, S) = (-1, 1)$. Horizontal axis: $k_r^*(1+h)$. Vertical axis: $k_i^*(1+h)$. The axes have been multiplied by $(1+h)$ in order to keep approximately the same number of saddle points in each figure. For strong confinement (small h), saddle points that correspond to the inner flow, s_{1a} and s_{1b}, are bunched around the k_i-axis and the highest saddle point, s_{2a}, corresponds to the outer flow. On the other hand at weak confinement (large h), saddle points that correspond to the outer flow, s_{2a} and s_{2b}, are bunched around the k_i-axis. This is seen even more clearly in figure 12. At intermediate values of h, there is strong interaction between the saddle points of the inner and outer flows which produces two combined modes with particularly high ω_i, which are denoted s_{c1} and s_{c2}.

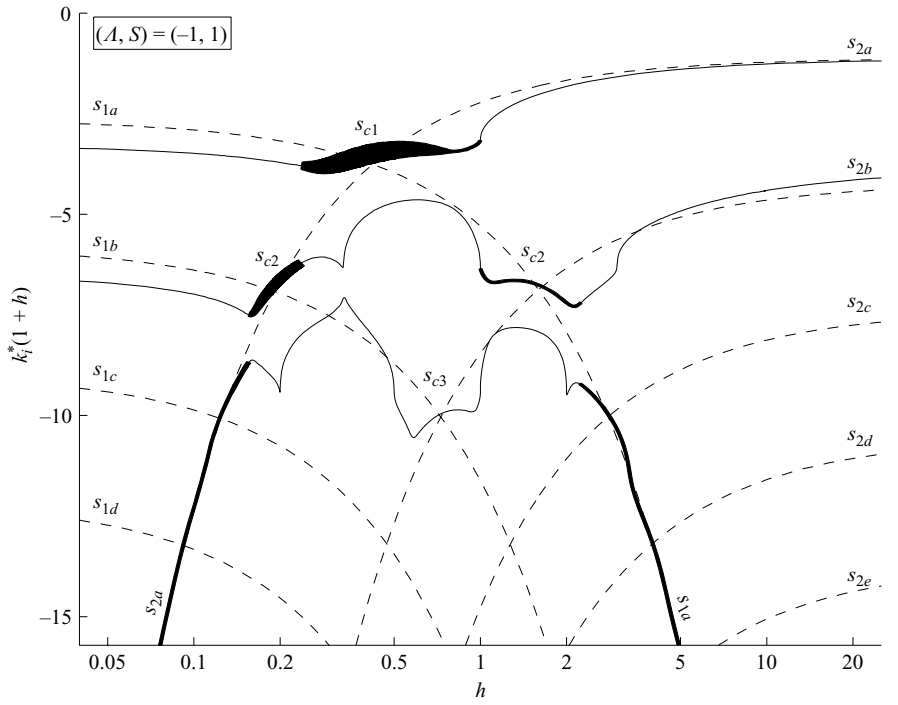

FIGURE 9. Solid lines: z-wavenumber, k_i, of the significant saddle points in figure 8, defined as the k^+/k^- pinch points that have the highest value of ω_i at some value of h. The line thickness increases with the absolute growth rate ω_i. Dotted lines: z-wavenumber, k_i, of the zero group velocity modes in the inner flow, s_{1a} to s_{1d}, and the outer flow, s_{2a} to s_{2e}. The combined flow has a higher absolute growth rate at values of h where the zero group velocity modes in the inner and outer flows have the same z-wavenumber. The mode with highest ω_i, called s_{c1}, arises when the two fundamental modes s_{1a} and s_{2a} coincide. The next most unstable combination, s_{c2}, arises when a fundamental coincides with a harmonic. The saddle formed by the coincidence of two harmonics, s_{c3}, always has lower ω_i than saddle s_{c1}.

Although some of the saddles that scale with the outer flow have higher ω_i, they have vanishing k_r when $h \gg 1$ and can be discounted for the reasons given in § 5.4. Consequently, saddle s_{1a} is the most unstable valid saddle point. The corresponding k^- branch has width $k_r \sim 1$ and is much wider than the k^- branches associated with the outer flow. These have width $k_r \sim 1/h$ and are bunched around the $k_r = 0$ axis. Physically, the wavelength of the dominant eigenfunction scales with the thickness of the inner flow and therefore dies down too quickly in the z-direction to be affected by the walls that confine the outer flow. As h decreases, this saddle point and its counterparts s_{1b}, s_{1c} and s_{1d} move along the dotted lines s_{1a}, s_{1b}, s_{1c} and s_{1d} in figure 9.

There is strong interaction between the inner and outer flows when $h \sim 1$, which can be seen on the manifolds presented in figure 8. At $h = 0.1$, saddle s_{2a} has the highest value of ω_i. As h increases, the fundamental mode in the outer flow, s_{2a}, interacts with the first harmonic of the inner flow, s_{1b}, forming saddles s_{c2} and s_{c3}. Saddle s_{c2} has the highest ω_i from $h = 0.155$ to $h = 0.235$. At larger h, the wavelength of the fundamental mode in the outer flow, s_{2a}, becomes similar to that of the fundamental mode in the inner flow, s_{1a}, forming saddle s_{c1}. This saddle has highest ω_i from $h = 0.235$ to $h = 1$. As h increases further, the wavelength in the outer flow increases and the first harmonic, s_{2b}, interacts with the fundamental of the inner flow, s_{1a}. This

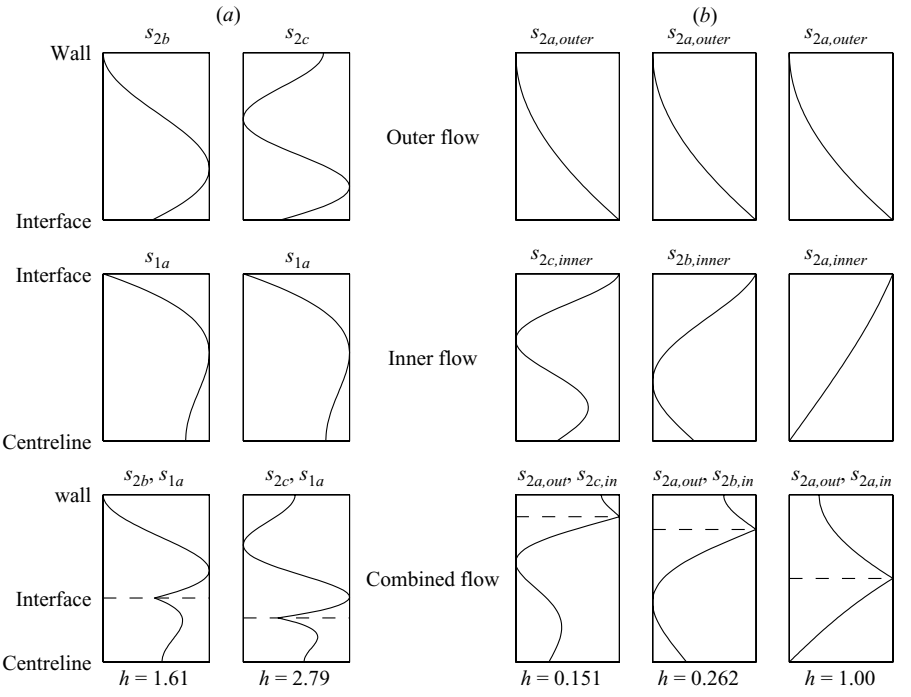

FIGURE 10. Mode shapes (pressure eigenfunctions) of zero group velocity modes in the following situations: top: in the outer flow in the limit of strong confinement; middle: in the inner flow in the limit of weak confinement; bottom: in the combined flow at values of h corresponding to strong interaction between these modes. In each case, we observe that the combined mode is indeed a combination of the other two modes. (a) Varicose, (b) sinuous motion.

saddle, s_{c2} again, has the highest ω_i from $h = 1$ to $h = 2.18$. At $h = 1.61$, the mode shapes of s_{2b} and s_{1a} can clearly be seen in the mode shape of the combined mode, as demonstrated in figure 10(a). Finally, saddle s_{1a} has the highest ω_i of the valid saddle points at large h. Thus, the saddle point with highest ω_i goes from being the fundamental mode of the outer flow to the fundamental mode of the inner flow via two saddle points with particularly high ω_i that arise because of resonance between the inner and outer flows.

The k_i-values of these saddle points (i.e. the wavenumber in the z-direction) are shown as solid lines in figure 9, where $k_i(1 + h)$ is plotted as a function of h. The saddle point with highest ω_i is shown as a bold line whose thickness increases with the growth rate, ω_i. The dotted lines in figure 9 are the k_i-values of the waves with zero group velocity that scale with the outer flow, s_{2a} to $_{s2d}$, and the inner flow, s_{1a} to s_{1d}, when uncombined. The combined flow is least stable (or most unstable) when the k_i-value of the combined instability is close to the intersection of these dotted lines, where the resonance between the two flows is strongly constructive. As shown in equation (5.1), these occur at $h = 0.092$, 0.124, 0.192, 0.420, 1.61, 2.79 and 3.98. Conversely, the flow is most stable at intermediate values of h, where the k_i-values of s_{2a} to s_{2d} fall between those of s_{1a} to s_{1d}. The most extreme example of this is at $h = 1$, where the two flows are no longer absolutely unstable to varicose perturbations for any amount of shear.

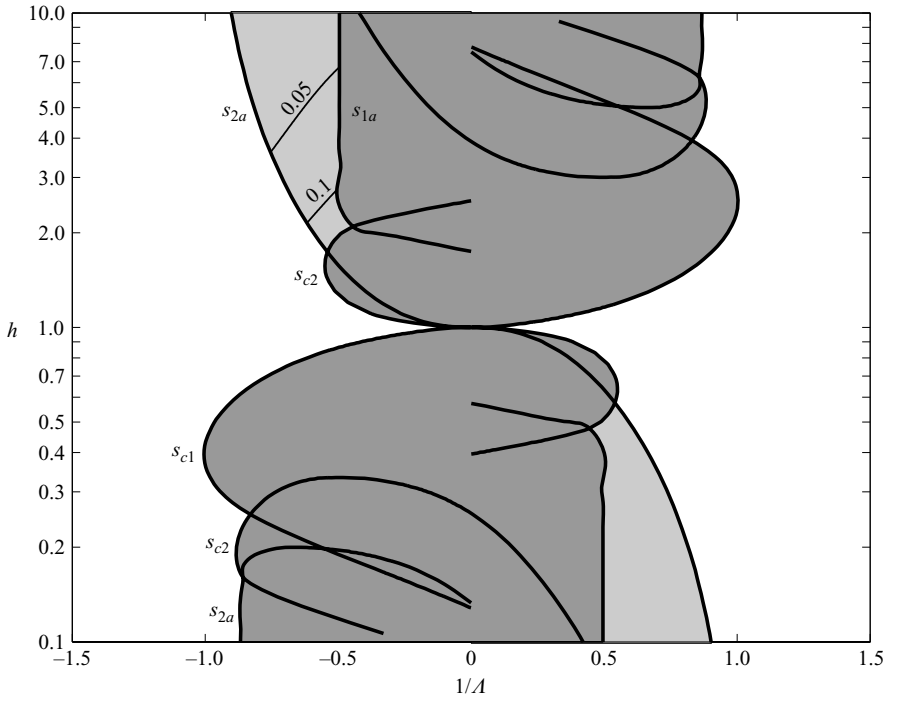

FIGURE 11. Areas of unambiguous absolute instability (dark grey) as a function of shear and confinement for a varicose motion with density ratio 1. The saddle point responsible for each transition line is indicated. The light grey region is due to saddle s_{2a}. Its absolute wavenumber, k_r, indicated by the contours 0.1 and 0.05, tends to zero as h tends to infinity. Thus, it is a region of ambiguous absolute instability described in § 5.4.

We can now understand the features of the map of absolute instability in the $(1/\Lambda, h)$ plane shown in figure 11. Confinement, h, is clearly affecting the amount of shear which is required to generate absolute instability. On the left-hand side of the figure, where the AI/CI transition line is at $\Lambda \sim -1$, there are local peaks of absolute instability around $h = 0.124$, 0.192, 0.420, 1.61, 2.79 and 3.98. This is expected because there are constructive interactions between zero group velocity modes in the inner and outer flows at these values of h. Under the symmetry $(\Lambda, h) \leftrightarrow (-\Lambda, 1/h)$, the corresponding values of h on the right-hand side of the figure are $h = 0.25$, 0.36, 0.62, 2.38, 5.21 and 8.06.

5.4. *Saddle points with small k_r*

Eigenvalues with very small values of k_r should be discounted on two physical grounds. First, a fundamental assumption of this analysis is that the base flow remains unchanged in the x-direction over distances of the order of a wavelength. Modes with small k_r would violate this assumption in any physical situation because they have very long wavelengths in the x-direction. Secondly, modes with small k_r die away very slowly in the z-direction. Their amplitudes must therefore tend to zero as k_r tends to zero in order to avoid having infinite energy. The cutoff value of k_r will depend on the rate at which the base flow varies in the x-direction and will be of order h_1/L, where L is a characteristic length scale of changes to the average flow in the x-direction. For the parallel flow assumption to be applicable, h_1/L of a physical configuration must be less than order 1.

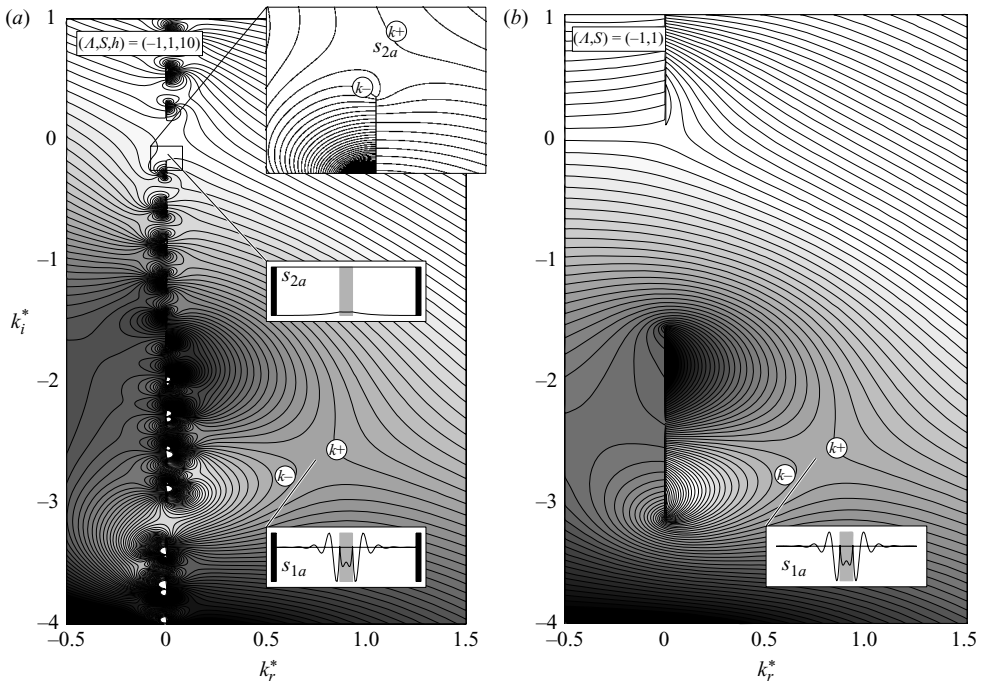

FIGURE 12. Contours of $\omega_i(k)$ for varicose perturbations in (a) weakly confined and (b) unconfined configurations. The relationship between the $k_r > 0$ regions of the two manifolds is clearly seen in this figure. The saddle point of the inner flow, s_{1a}, is in the same place on both manifolds. However, the saddle points of the outer flow, which are bunched around the k_i-axis in the confined case, do not exist in the unconfined case. Their wavenumbers, k_r, tend to zero as h tends to infinity. Consequently, saddle s_{2a} must be discounted as h tends to infinity even though it is the most unstable mathematically valid pinch point. This is explained in detail in § 5.4.

There is a set of k^+/k^- pinch points that are always valid because their k_r values are always of order 1. These are called normal saddle points. There is another set of k^+/k^- pinch points whose k_r values tend to zero as h tends to infinity. This is demonstrated in figure 12 which plots (a) the confined case with $h = 10$ alongside (b) the unconfined case at the same density ratio and shear. Although saddle s_{2a} is a mathematically valid k^+/k^- pinch point, it has vanishing k_r as h tends to infinity and must be discounted for the reasons described above. This is verified by the fact that it does not exist at all in the unconfined case, where the only k^+/k^- pinch point is saddle s_{1a}. Nevertheless, this pinch point cannot be discounted completely because it has a significant value of k_r when $h \sim 1$. We shall see in § 7 that the k_r values of saddle points such as s_{2a} can reach order 1 at different parameter values. These are called ambiguous saddle points because they are mathematically valid, but must be discounted below k_r of order h_1/L for physical reasons.

As an example, when $(\Lambda, h) = (-2, 2)$, saddle s_{2a} is the only saddle with positive growth rate and has $k_r = 0.12$. In a physical system, it is ambiguous whether saddle s_{2a} would cause the flow to be absolutely unstable or whether its long wavelength would violate the assumption of an unchanging base flow. The region of ambiguous absolute instability swept out by saddle s_{2a} in the $(1/\Lambda, h)$-plane is shown in light grey in figure 11 together with contours of k_r for this mode.

This type of saddle point has been noticed before. Delbende & Chomaz (1998) numerically calculate the fully nonlinear impulse responses of a weakly confined wake flow with $(\Lambda, S, h) = (-1, 1, 12.8)$. They show that k_r at the leading edge of the unstable wave packet tends to zero (their figure 12). These authors also examine a confined wake flow with $(\Lambda, S, h) = (-1, 1, 2.4)$. In this case (their figure 8), the k_r value does not tend to zero. Both of these results concur with the results of this study.

6. Effect of confinement on sinuous perturbations of a double shear layer in a uniform fluid

Following the same process as that in § 5, we can show that confinement has an even stronger effect on sinuous perturbations. The dispersion relation for sinuous perturbations of the double shear layer in a uniform fluid is:

$$D \equiv (U_1 - \omega/k)^2 \tanh(kh_1) + (U_2 - \omega/k)^2 \coth(kh_2) = 0. \tag{6.1}$$

This can be rearranged to reveal an obvious symmetry under the transformation $h_1 \leftrightarrow h_2$, which in non-dimensional terms is $h \leftrightarrow 1/h$:

$$\frac{(U_1 - \omega/k)^2}{(U_2 - \omega/k)^2} = -\coth(kh_1)\coth(kh_2).$$

A confined sinuous flow with $\Lambda = -1$ is examined here. When $h \ll 1$ (strong confinement), the flow has the same image system as figure 7(*c*). Thus, the behaviour is the same as that of the strongly confined varicose flow with $\Lambda = -1$. This can also be seen in the dispersion relation (6.1) since $\tanh(kh_1)$ tends to 1, leaving the $\coth(kh_2)$ term that is characteristic of varicose disturbances. It was shown in § 5 that the behaviour of the strongly confined varicose flow with $\Lambda = -1$ is the same as that of the unconfined varicose flow with $\Lambda = +1$. Hence when there is strong confinement, the modes with zero group velocity that have highest ω_i scale with the outer flow and are saddle points s_{2a} to s_{2d} in figure 4(*a*). These saddle points lie at $k_{i,outer} = -(1.113 + n\pi)/h_2$, $n = 0, 1, 2$ etc. As h varies, they trace out the lines $s_{2a,outer}$ to $s_{2d,outer}$ in figure 13.

When $h \gg 1$ (weak confinement), we can use the fact that the dispersion relation is symmetric under $h \to 1/h$. Thus the weakly confined sinuous flow with $\Lambda = -1$ has the same eigenvalues as the strongly confined sinuous flow with $\Lambda = -1$ and hence the same eigenvalues as the unconfined varicose flow with $\Lambda = +1$. The eigenvalues with zero group velocity are also saddle points s_{2a} to s_{2d}, but the corresponding eigenfunctions are antisymmetric rather than symmetric. These saddle points scale with the thickness of the inner flow and lie at $k_{i,inner} = -(1.113 + m\pi)/h_1$, $m = 0, 1, 2$, etc. As h varies, they trace out the lines $s_{2a,inner}$ to $s_{2d,inner}$ in figure 13.

The manifold of the confined sinuous flow has similar general features to that of the confined varicose flow and will not be described here. In figure 13, which has exactly the same scale as figure 9, the k_i-values of the relevant saddle points are shown as functions of h. The most unstable saddle point is shown in bold, with the line thickness increasing with ω_i. As h increases, the most unstable saddle point goes from being the fundamental mode of the outer flow, $s_{2a,outer}$, to the fundamental mode of the inner flow, $s_{2a,inner}$, via two saddle points at much higher ω_i: s_{c2} and s_{c1}. These saddles arise because of resonance between the inner and outer flows. This is the same process as that observed in the confined varicose flow with $\Lambda = -1$ but, as can be seen by comparing the thickness of the lines in figures 9 and 13, the confined sinuous

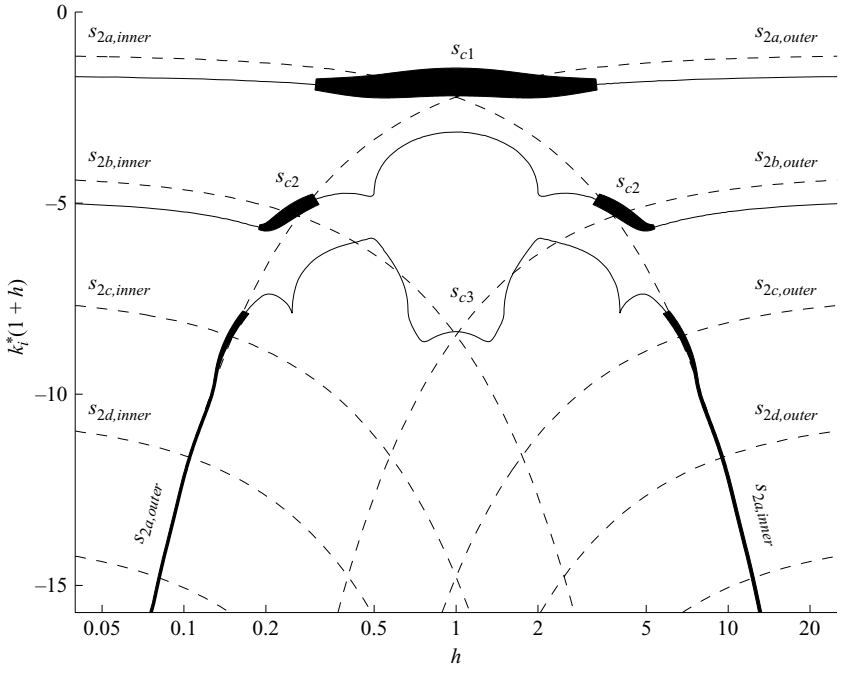

FIGURE 13. Solid lines: z-wavenumber, k_i, of the significant saddle points of a confined sinuous wake flow with $(\Lambda, S)=(-1, 1)$. The line thickness increases with the absolute growth rate ω_i. Dotted lines: z-wavenumber, k_i, of the zero group velocity modes in the inner flow, $s_{2a,inner}$ to $s_{2d,inner}$, and the outer flow, $s_{2a,outer}$ to $s_{2d,outer}$. The combined flow has higher ω_i at values of h where the zero group velocity modes in the inner and outer flows have the same z-wavenumber. The most unstable flow arises when the two fundamental modes $s_{2a,outer}$ and $s_{2a,inner}$ coincide. The scale is identical to that in figure 9, revealing that the sinuous motion at $(\Lambda, S)=(-1, 1)$ is considerably more unstable than the varicose motion.

flow with $\Lambda=-1$ is more unstable. At this value of S, there are no ambiguous saddle points.

Constructive interaction between the the inner flow and the outer flow is expected when $k_{i,inner}=k_{i,outer}$, which occurs at:

$$\Rightarrow h \equiv \frac{h_2}{h_1}=\frac{1.113+n\pi}{1.113+m\pi}=0.106, 0.151, 0.262, 1.00, 3.82, 6.65, 9.46\ldots$$

From inspection of figures 13 and 14, we can see that these points do indeed correspond to local instability maxima around $\Lambda=-1$. The strongest instability is when the two fundamentals interact constructively at $h=1$. As for the varicose case, this interaction can clearly be seen in the mode shapes in figure 10(b).

7. Effect of shear, density ratio and confinement on varicose and sinuous perturbations

The analysis in §§ 5 and 6 can be repeated at different density ratios, S. The manifold defined by $D(\omega, k; \Lambda, S, h)=0$ has the same general features as the case with $S=1$. The chief difference is that the k^- branches that scale with the outer flow have width $k_r \sim 1/(Sh)$, while those that scale with the inner flow have width $k_r \sim 1$. Hence as the density of a flow increases, the widths of that flow's associated

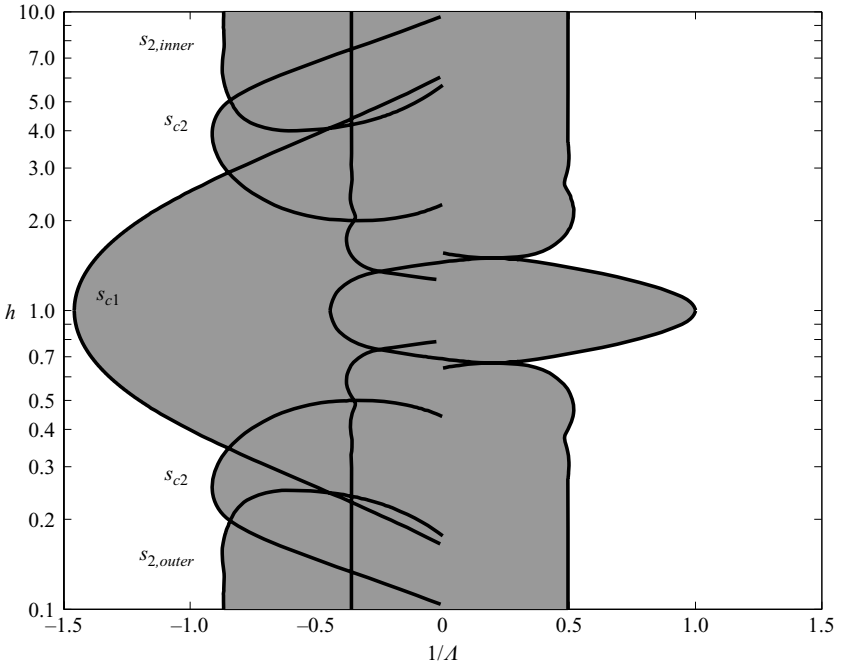

FIGURE 14. Areas of unambiguous absolute instability (dark grey) as a function of shear and confinement for a sinuous motion with density ratio 1. The saddle point responsible for each transition line is indicated. The scale is the same as that in figure 11.

k^- branches increase relative to those of the other flow, causing its corresponding saddle points to become more unstable. Thus, the convective/absolute transition tends to be more influenced by the denser flow than by the lighter flow.

Figure 15 shows the effect of shear, density ratio and confinement on varicose perturbations. The top left-hand figure shows the effect of shear and density ratio on the unconfined case and is a repeat of figure 6. The remaining seven figures, which are slices through the top left-hand figure, show the effect of shear and confinement at different density ratios. The dark grey regions are absolutely unstable – they are swept out by normal saddle points such as s_{c2} and have wavenumbers $k_r \sim (1+h)$. The light grey regions are ambiguously absolutely unstable – they are swept out by ambiguous saddle points such as s_{2a} that are described in § 5.4. Contours of the wavenumber, k_r, are shown for these saddle points. The white regions are convectively unstable.

The behaviour at a density ratio of $S = 0.001$ can be explained in four parts. (i) As $h \to \infty$ the inner flow dominates the behaviour and the dark grey region of absolute instability matches that of the unconfined case. The light grey region of ambiguous absolute instability is caused by saddle s_{2a}, a mode that corresponds to the outer flow. Its wavenumber tends to zero and it must be discounted owing to the physical argument in § 5.4. (ii) In the range $1 < h < 2$, the ambiguous saddle has a wavenumber of around 0.4 and can probably not be discounted on physical grounds (this depends on the value of the cutoff wavenumber described in § 5.4). If valid, the ambiguous saddle will dominate the behaviour, except around $\Lambda = 1$ where the combined mode s_{c2} dominates. (iii) In the range $0.35 < h < 1$, the combined mode s_{c1} dominates. (iv) As $h \to 0$, the outer flow dominates the behaviour. The outer flow is both denser and slower so the dark grey region of unambiguous absolute instability is larger than

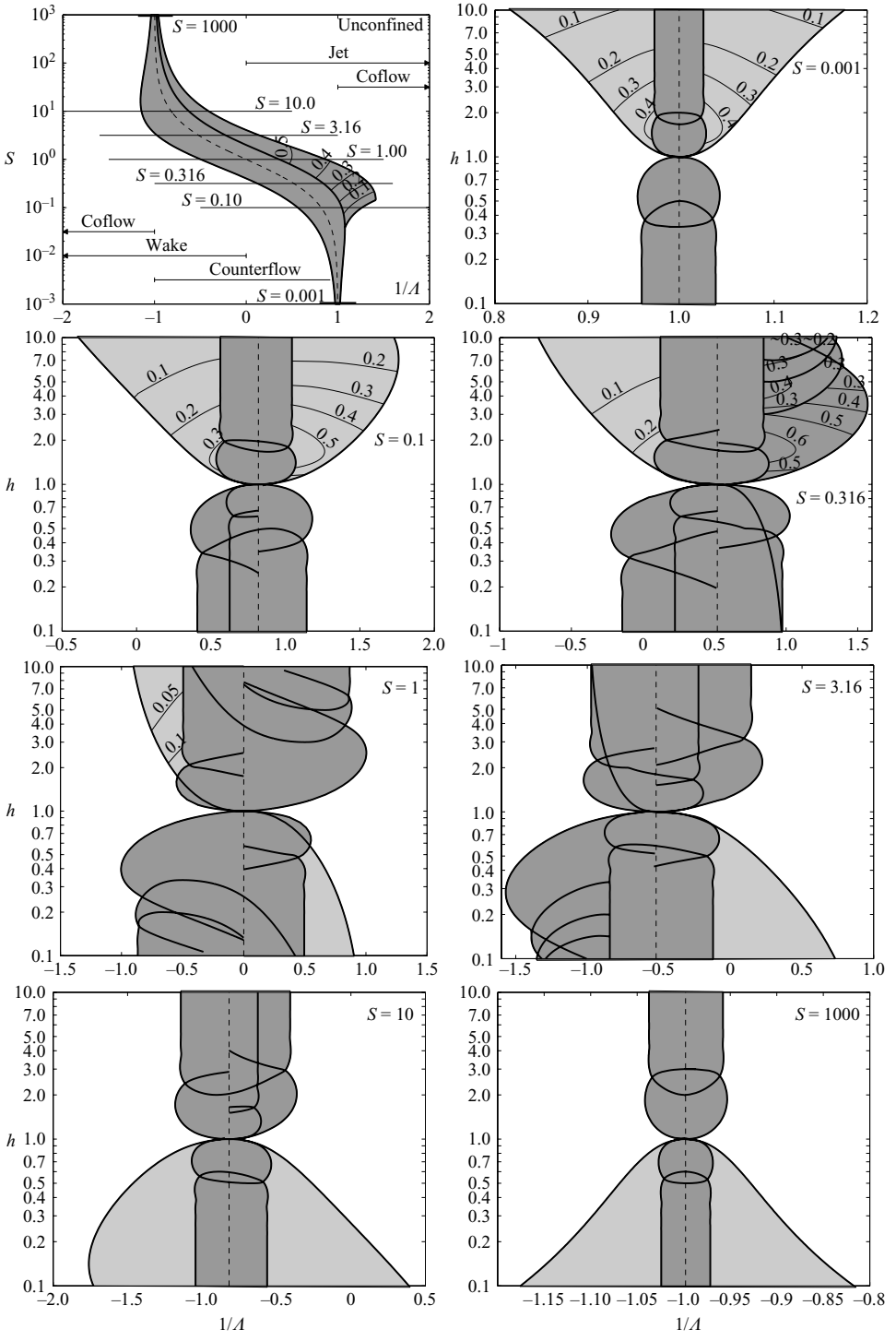

FIGURE 15. Absolute instability for varicose motion of a confined shear flow as a function of shear, density ratio and confinement. The top left-hand figure is the unconfined case. The remaining figures are in the $(1/\Lambda, h)$-plane at given density ratios. Regions of unambiguous absolute instability are shown in dark grey. Regions of ambiguous absolute instability are in light grey, showing contours of k_r. Zero net mass flux, $\rho_1 U_1 + \rho_2 U_2 = 0$, is shown by the dotted line. Note that the scales on the horizontal axes differ.

when the inner flow dominates the behaviour. There is no ambiguously absolutely unstable region for $h < 1$ at this density ratio.

At density ratios of $S = 0.1$ and 0.316 the behaviour of the normal saddle points is similar to that at $S = 0.001$. However, the ambiguous saddle points have more curious behaviour. On the left-hand side of the dotted line, the ambiguous saddle point's wavenumber tends to zero as h tends to infinity, as before. However, on the right-hand side of the dotted line, there are now several saddle points and the wavenumber of the most unstable does not tend to zero as h tends to infinity. For example, the envelope of saddle points at $S = 0.316$ tends to a minimum value of $k_r = 0.2$ as h tends to infinity because there is a corresponding saddle point at $k_r = 0.2$ in the unconfined case. Furthermore, the ambiguous saddle point on the right-hand side of the dotted line when $S = 0.001$ changes smoothly into a normal saddle point as S increases to 1000. This is curious behaviour and a precise description of these ambiguous saddle points remains to be determined. Finally, the behaviour at $S > 1$ can be found from the symmetry $(\Lambda, S, h) \leftrightarrow (-\Lambda, 1/S, 1/h)$.

Figure 16 shows the effect of shear, density ratio and confinement on sinuous perturbations. At $S = 0.001$, we observe the increased instability of the combined saddle s_{c1} around $h = 1$, where the fundamental modes of the inner and outer flows have the same wavenumber. As S increases, saddle s_{c1} becomes extremely unstable and extends the absolutely unstable region far to the left. This means that for density ratios $S \geqslant 1$, confined wakes are absolutely unstable, even with strong co-flow. However, as the density ratio increases, s_{c1} changes smoothly into an ambiguous saddle point. Its wavenumber tends to zero and it must eventually be discounted on physical grounds. Again this depends on the value of the cutoff wavenumber described in § 5.4. The symmetry transform in the sinuous case is $(\Lambda, S, h) \leftrightarrow (\Lambda, S, 1/h)$, which can clearly be seen in the figures.

8. Conclusions, implications and further work

This work has examined the effect of confinement on the convective/absolute transition of two-dimensional jets and wakes. The analysis locates the modes of zero group velocity via a geometrical method. Distinct modes exist in both the inner and outer streams in the limit of weak and strong confinement. When the flows have similar thicknesses, modes in the inner flow interact constructively with modes in the outer flow if their z-wavenumbers, k_i, are similar. This makes the combined flow more unstable than the individual flows would be without any confinement. The results presented here show the level of confinement, h, that leads to the strongest absolute instability over a large range of density ratios. However, in some flow regimes, the wavenumber of the most unstable mode tends to zero and it must be discounted on physical grounds. This study cannot determine the cutoff wavenumber at which the mode ceases to be active, so cannot determine the exact region of absolute instability in these particular flow regimes.

This study implies that by confining parts of a wake or a jet one can create regions of local absolute instability surrounded by regions of local convective instability. This has some scientific implications. For instance Pier & Huerre (2003) have shown numerically that the frequency of a global mode in a smoothly developing wake flow is dictated by the frequency of the upstream point of absolute instability. An experiment or a numerical analysis of a partly confined wake could generate several such pockets of absolute instability, each with different local frequencies. It would be

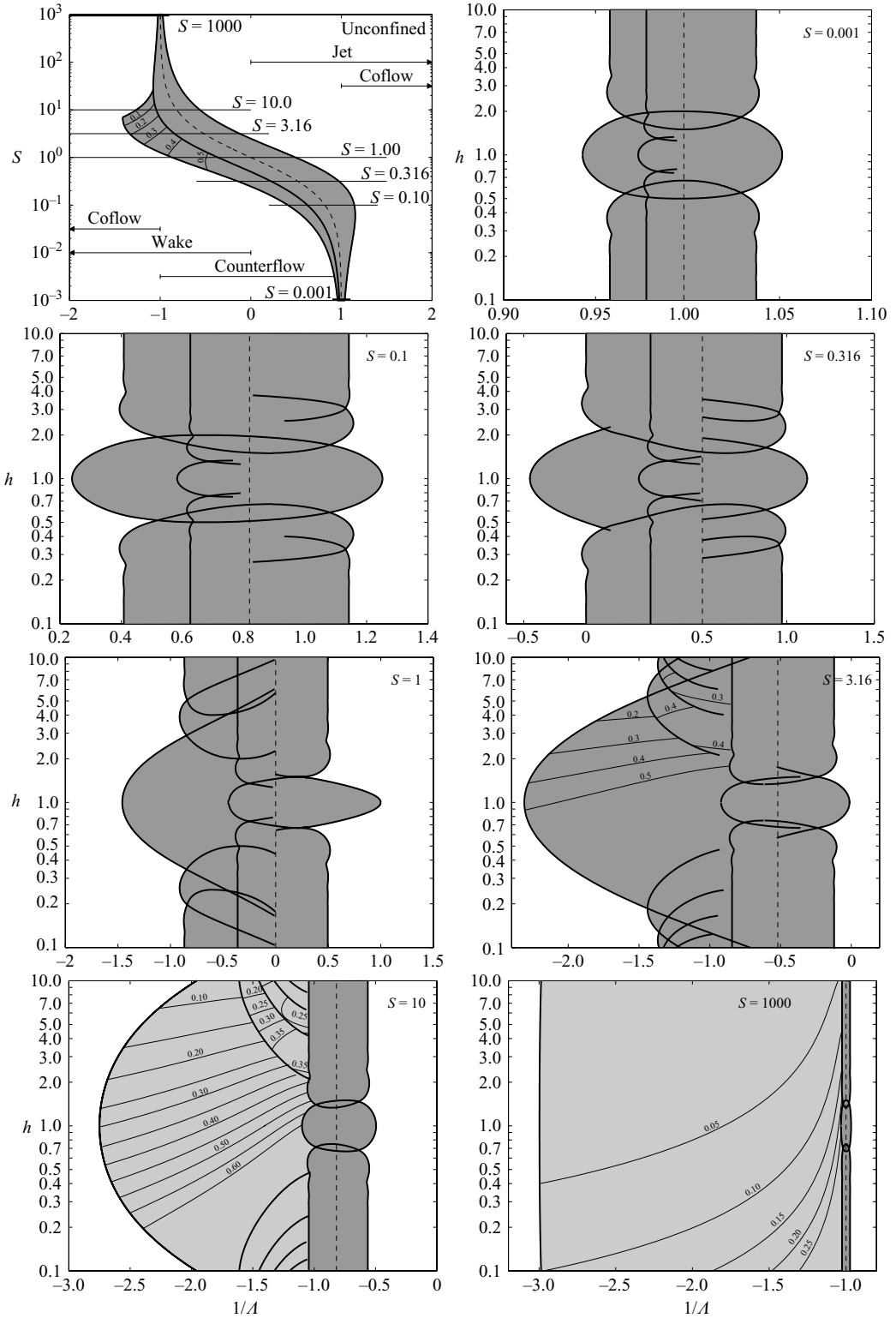

FIGURE 16. As for figure 15, but for sinuous motion.

interesting to see whether the global mode corresponded to the most upstream pocket or whether it could be made to respond to a downstream pocket.

It has consistently been found through trial and error that confined shear injectors are a good configuration for industrial injection systems which require good mixing with a low pressure drop. It is likely that this is because they stimulate an unstable global shear mode whose large-scale flapping or spiralling motion enhances mixing. This article presents useful first-order design rules for such injectors, such as the optimum configuration for a given density ratio. More useful design rules will emerge from axisymmetric models.

This work can be extended to the axisymmetric confined configuration. When there is no swirl, the manifold for perturbations with zero azimuthal wavenumber, m, is very similar to the two-dimensional varicose manifold. Likewise, the manifold with $m = 1$ is very similar to the two-dimensional sinuous manifold. Higher azimuthal wavenumbers are always more stable than $m = 0$ and $m = 1$ with the exception of $m = 2$ at a very specific value of confinement and shear. Thus, the regions of absolute instability in the axisymmetric confined configuration are very similar to those in the two-dimensional confined configuration. However, when the flows also have an azimuthal velocity, the resultant centrifugal modes interact with the Kelvin–Helmholtz modes and the behaviour becomes quite different, as shown by Loiseleux, Chomaz & Huerre (1998). The results of the axisymmetric configuration will be reported in a future paper.

REFERENCES

Barrère, M., Jaumotte, A., Fraeijs de Veubeke, B. & Vandenkerckhove, J. 1960 *Rocket Propulsion*. Elsevier.

Bearman, P. & Zdravkovich, M. 1978 Flow around a circular cylinder near a plane boundary. *J. Fluid Mech.* **89**, 33–47.

Briggs, R. 1964 *Electron-Stream Interaction with Plasmas*. MIT Press.

Chomaz, J.-M. 2005 Global Instabilities in spatially developing flows: non-normality and nonlinearity. *Annu. Rev. Fluid Mech.* **37**, 357–392.

Delbende, I. & Chomaz, J.-M. 1998 Nonlinear convective/absolute instabilities in parallel two-dimensional wakes. *Phys. Fluids* **10**, 2724–2736.

Drazin, P. & Reid, W. 1981 *Hydrodynamic Stability*. Cambridge University Press.

Huerre, P. 2000 Open shear flow instabilities. In *Perspectives in Fluid Dynamics: a Collective Introduction to Current Research* (eds. G. K. Batchelor, H. K. Moffat & M. G. Worster). Cambridge University Press.

Huerre, P. & Monkewitz, P. 1990 Local and global instabilities in spatially developing flows. *Annu. Rev. Fluid Mech.* **22**, 473–537.

Juniper, M. & Candel, S. 2003 The stability of ducted compound flows and consequences for the geometry of coaxial injectors. *J. Fluid Mech.* **482**, 257–269.

Loiseleux, T., Chomaz, J. & Huerre, P. 1998 The effect of swirl on jets and wakes: linear instability of the Rankine vortex with axial flow. *Phys. Fluids* **10**, 1120–1134.

Pier, B. & Huerre, P. 2003 Nonlinear self-sustained structures and fronts in spatially developing wake flows. *J. Fluid Mech.* **435**, 145–174.

Shair, F., Grove, A., Petersen, E. & Acrivos, A. 1963 The effect of confining walls on the stability of the steady wake behind a circular cylinder. *J. Fluid Mech.* **17**, 546–550.

Yu, M.-H. & Monkewitz, P. 1990 The effect of nonuniform density on the absolute instability of two-dimensional inertial jets and wakes. *Phys. Fluids* A **2**, 1175–1181.